Particle Accelerators, 1996, Vol. 53, pp. 35–52
Reprints available directly from the publisher
Photocopying permitted by license only

THERMOMETRIC STUDY OF ELECTRON EMISSION IN A 1.3 GHz SUPERCONDUCTING CAVITY

M. PEKELER,[1] T. FULJAHN,[1] P. SCHMÜSER,[1] H. PADAMSEE,[2] M. CHAMPION,[3] C. CRAWFORD,[3] J. GRABER,[3] A. MATHEISEN,[3] W.-D. MÖLLER[3] and D. PROCH[3]

[1]*II. Institut für Experimentalphysik der Universität Hamburg, Notkestrasse 85, 22603 Hamburg, Germany*

[2]*Laboratory of Nuclear Studies, Cornell University, Ithaca, NY 14853–5001, USA*

[3]*Deutsches Elektronen Synchrotron DESY, 22603 Hamburg, Germany*

(Received 11 January 1996; in final form 11 January 1996)

A 768-thermometer temperature mapping system with 40 ms total readout time was used for field emission studies on a single-cell 1.3 GHz niobium cavity, immersed in superfluid helium. Any significant change in the excitation function $Q(E)$ of the cavity (quality factor as function of accelerating field) could be associated with a modification in the temperature map. The energy deposition by field-emitted electrons was studied as a function of position on the cavity surface. The removal of field emitters by high peak power processing (HPP) was clearly visible on the temperature map. HPP improved the attainable gradient but in several cases reduced the low-field Q of the cavity, probably due to surface contamination by material evaporated from the processed emitter.

Keywords: Superconducting cavity, field emission, thermionic emission, temperature mapping, high peak power processing

1 INTRODUCTION

The TESLA design for a linear electron-positron collider in the 500 GeV to 1 TeV centre-of-mass energy regime is based on 9-cell 1.3 GHz superconducting niobium cavities with an accelerating field of 25 MV/m. This value, although considerably lower than the theoretical maximum of about 50 MV/m, is more than a factor of two above present-day standards.[1]

The main limitations are due to thermal breakdown and field emission of electrons from the inner surface. A temperature mapping system is well suited to localize hot spots on the inner cavity surface and furthermore it can be utilized to study the properties of field emitters and the effect of high peak power processing.

2 EXPERIMENTAL PROCEDURE

The experiments were performed on a single-cell cavity with slightly elliptic cross section, built at Cornell University. Niobium with an initial residual resistivity ratio $RRR = 250$ was used and the cavity was heat-treated at 1400°C with solid state gettering by titanium from the outside to raise the RRR to 350. A layer of about 100 μm was removed from the inner surface by buffered chemical polishing (BCP 1:1:2). After that the cavity reached an accelerating gradient of 26 MV/m at Cornell. Prior to the RF tests at DESY, the inner surface was etched (15 μm), rinsed with de-ionized water and finally cleaned by high pressure water rinsing. The cavity was dried in a class 10 clean room and then mounted in a vertical test stand. Small vacuum leaks at the input-coupler side required replacement of Helicoflex seals in the two test series described below. It was decided to proceed with the tests without removing possible contaminants due to the leaks. The temperature maps in fact revealed some particle contamination of the cavity surface which, however, turned out useful for exploiting the capabilities of the diagnostic system.

In the vertical dewar the RF power is guided into the cavity through a rectangular 1.3 GHz waveguide with a door-knob like transition to a coaxial input coupler. For continuous wave (cw) operation a 250 W solid state amplifier is used while high peak power processing (HPP) is performed with a 4 MW klystron with a maximum pulse length of 2 ms. The highest power the cavity was exposed to during HPP was 700 kW. The cavity is bath-cooled with superfluid helium of 1.5 K.

A temperature mapping system was built at Cornell University and DESY, following a design for 1.5 GHz cavities.[2] It consists out of 768 spring-loaded thermometers (see Figure 1a) whose basic component is a 100 Ω Allen-Bradley carbon resistor (room temperature value). In liquid helium the resistance is strongly temperature dependent, ranging from 1000 Ω at 4 K to about 15 kΩ at 1.5 K.

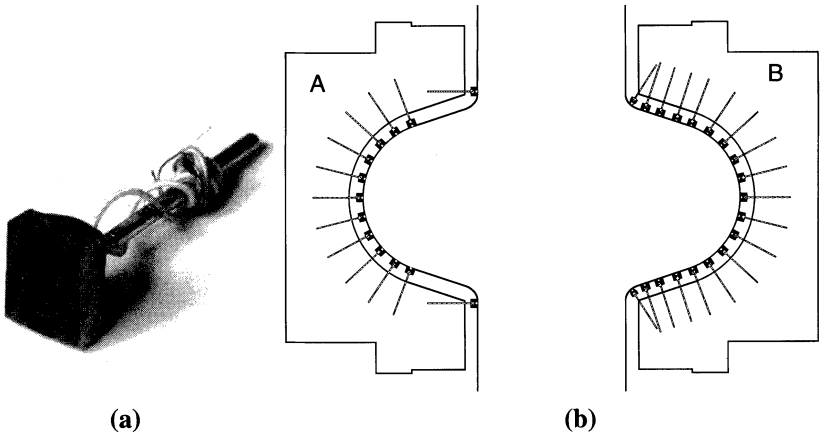

FIGURE 1 (a) Thermometer of the temperature mapping system. (b) Schematic drawing of the two different thermometer boards.

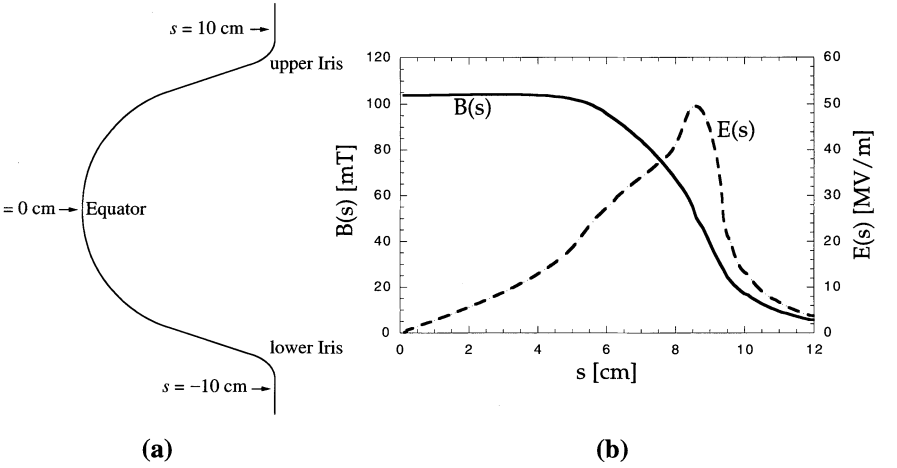

FIGURE 2 (a) Definition of the coordinate s along a meridian. (b) Local magnetic field $B(s)$ and local electric field $E(s)$ as a function of s. The values are calculated for an accelerating gradient of $E_{acc} = 25$ MV/m.

To improve the thermal contact, Apiezon N grease is used which effectively prevents superfluid helium from penetrating the gap between thermometer and cavity surface. The thermometers are mounted on printed circuit boards of two different types (see Figure 1b) to achieve optimum coverage of the cavity

surface including the beam tube sections. Each board covers a meridian of the cavity. A coordinate s along the meridian is defined according to Figure 2a, the upper and lower iris are at $s = \pm 10$ cm while the equator is at $s = 0$. The azimuthal angle between adjacent boards is 7.5°; there are 24 boards with 19 thermometers each and 24 boards with 13 thermometers. The resistors are fed with a constant current of 10 μA and the voltages are guided out of the cryostat via parallel cables and connectors at the vacuum flange to type NI-SCXI-1100 multiplexers and a NI-MIO-16XL analog-to-digital converter. The thermometers are read out sequentially, the total readout time being 40 ms.

Data collection and analysis is performed using LabVIEW on a Macintosh Quadra 950 computer. During cooldown from 4.2 K to 1.5 K all thermometers are individually calibrated at 0.1 K intervals against the temperature derived from the helium vapour pressure. The helium bath temperature T as a function of resistance R is parametrized in the form

$$\frac{1}{T} = \sum_{i=0}^{4} a_i (\ln R)^i . \tag{1}$$

The resolution is in the order of 2 mK.

To create a temperature map of the cavity surface, readings with and without RF field in the cavity are made and then subtracted. Besides temperature maps of the entire cavity, selected boards can be read out at higher repetition rate. This permits the study of transient heating at field-emitting locations.

The response of the thermometers to heating of the inner cavity surface is determined experimentally by measurements at low fields. As long as no electron emission is present in the cavity, the dissipated power P_{diss} per unit area, which can be derived from the incident and reflected RF power, is deposited rather uniformly over the cavity surface. The average temperature rise $\langle \Delta T \rangle$ of all thermometers is found to increase linearly with P_{diss}. From these data we have determined the average thermometer sensitivity:

$$\eta_{\mathrm{th}} = \langle \Delta T \rangle / P_{\mathrm{diss}} = 2 \cdot 10^{-4} \ \mathrm{K/(W/m^2)} \tag{2}$$

which should be accurate to within a factor of 2 (a more precise calibration has not been possible because the heat transfer coefficient between cavity surface, Apiezon grease and carbon resistor is extremely sensitive to small amounts of superfluid helium penetrating the gap).

3 FIELD LIMITATIONS IN SUPERCONDUCTING CAVITIES

3.1 Thermal Breakdown

The high-frequency magnetic field induces eddy currents of the normal (non-superconducting) electrons in a surface layer about London penetration length deep. A thermal breakdown or quench may start in a region of increased surface resistance, either a normal-conducting zone, a defect or a foreign particle. If more heat is generated than can be conducted away through the bulk material into the surrounding superfluid helium bath, the normal area starts to grow, thereby producing more and more heat, until the whole stored energy of the cavity is dissipated in the warm region. A high thermal conductivity of the wall material is essential for avoiding thermal breakdown at low field levels.

The power density generated by the eddy currents is proportional to the square of the local magnetic field. The strength of the local magnetic field $B(s)$ along a meridian is plotted in Figure 2b; $B(s)$ has its peak value B_p at the equator at $s = 0$ and drops rather slowly towards the iris.

An example of eddy-current heating in an area of increased surface resistance is shown in Figure 3. The temperature map (Figure 3a) reveals a warmer zone near the equator at an azimuthal angle of 270°. The temperature rise in the area is plotted in Figure 3b as a function of B^2, where B is the local field. The parabolic law is very well obeyed.

3.2 Field Emission

Field emission of electrons via the quantum-mechanical tunnel effect depends exponentially on the local electric field $E(s)$ which may be strongly enhanced at small tips or sharp edges. Assuming a smooth cavity surface the local electric field has been calculated using the finite-element code SUPERFISH. In Figure 2b $E(s)$ is plotted as a function of the coordinate s along a meridian; the numbers refer to an accelerating field on the cavity axis of $E_{\mathrm{acc}} = 25$ MV/m. The local electric field vanishes at the equator and has a pronounced peak near the iris with $E_{\mathrm{peak}} = 1.98 \cdot E_{\mathrm{acc}}$. Hence field emission should predominantly occur in this region. The electron current density is given by the Fowler-Nordheim equation

$$j_{\mathrm{FE}} = c_1 E^{2.5} \exp\left(-\frac{c_2}{\beta E}\right). \tag{3}$$

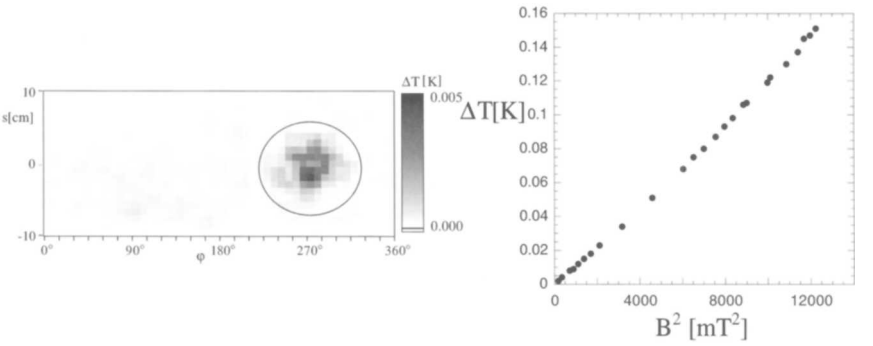

(a) **(b)**

FIGURE 3 (a) Unfolded temperature map of the cavity at an accelerating field of 2.5 MV/m. Circled is an area with high surface resistance. (b) Heating ΔT of the hottest thermometer as a function of the square of the local magnetic field B.

Here c_1 and c_2 are constants and $E \equiv E(s)$ denotes the computed local field (assuming a smooth surface). In comparison with field emission from a planar metal surface in a d.c. electric field there are two modifications:

1. A so-called *field enhancement factor* β is introduced as an adjustable parameter to account for the fact that field emission usually proceeds at small tips or sharp edges where the field is strongly enhanced; typical values are $\beta = 100 - 500$.
2. Field emission in RF fields is characterized by a factor $E^{2.5}$ in front of the exponential instead of the well-known E^2 factor in d.c. fields.

The electrons are accelerated in the RF electric field and extract energy from the cavity, thereby reducing its quality factor. A question of great concern is where they impinge on the wall and deposit their kinetic energy in the form of heat. Since the electric field has no azimuthal component, the trajectories emerging from a point source are confined to the plane defined by the meridian on which the emitting site is located and the centre axis of the cavity. The exponential factor in Equation (3) has the consequence that field emission occurs only in a limited interval of the RF phase (about $(90\pm25)^\circ$ for a sinosoidal time dependence of the surface electric field $E(t) = E_0 \sin \omega t$). This has a significant impact on the trajectory pattern.

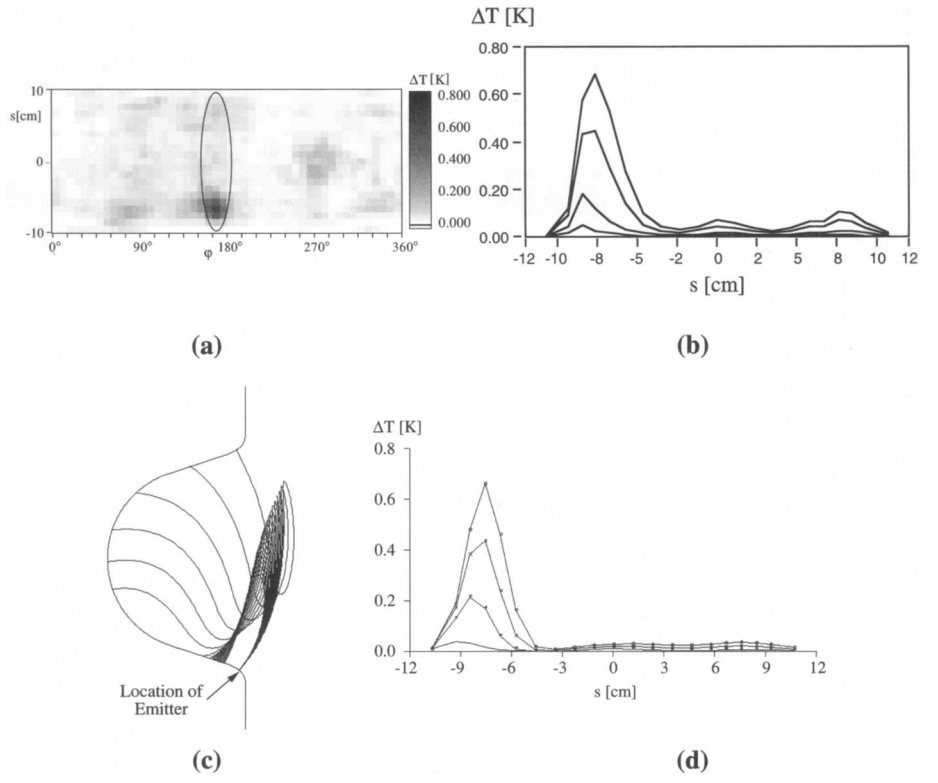

FIGURE 4 (a) Temperature map with a candidate for field emission. (b) Measured temperature distribution of the field emitter for 4 electric field levels (E_{acc} = 9.4, 11.4, 12.6 and 13.4 MV/m). (c) Computed trajectories from electrons emitting out of a field emitter at a phases (90 ± 25)° of the RF field of E_{acc} = 13.4 MV/m. The emitter is located at $s = -8.73$ cm. (d) Calculated heating of the outer surface for the electrons leaving the field emitter at $s = -8.73$ cm. The same electric field levels as in (b) are used.

A good candidate for a field emitting site is found in the temperature map of Figure 4a where a hot spot is observed at an azimuthal angle $\varphi = 170°$ and $s = -8$ cm. The measured temperature distribution along the $\varphi = 170°$ meridian is plotted in Figure 4b for accelerating fields of 9.4, 11.4, 12.6 and 13.4 MV/m. Figure 4c shows the computed electron trajectories for a supposed field emitter at $s = -8.73$ cm and for an accelerating field of 13.4 MV/m. A remarkable feature is that the majority of the electrons hit the cavity close to the emitting site. The energy deposited by the accelerated

electrons is translated into a temperature rise ΔT of the thermometers by using the sensitivity factor η_{th}. The computed ΔT distribution obtained in this manner is depicted in Figure 4d. The measured and calculated temperature distributions are very similar. Both exhibit a pronounced peak near the location of the field emitter. With increasing field the peak moves towards the equator. From the good agreement we draw the conclusion that the observed heating in Figures 4a and 4b is indeed caused by field emission.

3.3 Thermionic Emission

Foreign particles sticking to the inner surface with poor thermal contact to the bulk material can be eddy-current heated to temperatures where thermionic electron emission takes place. The hot particle emits a current density given by the Richardson equation

$$j_{\text{TE}} = c_3 T^2 \exp\left(-\frac{\Phi}{k_B T}\right). \tag{4}$$

Here c_3 is a constant, Φ is the work function of the emitting particle and k_B the Boltzmann constant. The temperature T of the emitter increases with the square of the local magnetic field $B(s)$ which in turn is proportional to the magnitude E_0 of the local electric field. Introducing new constants c_4, c_5 the thermionic current density can also be written as

$$j_{\text{TE}} = c_4 E_0^4 \exp\left(-\frac{c_5}{E_0^2}\right). \tag{5}$$

A temperature map with a candidate for a thermionic emitter at $\varphi = 340°$ and $s = -7.2$ cm is presented in Figure 5a. The measured temperature distribution along the meridian is shown in Figure 5b for fields of $E_{\text{acc}} = 11.5$, 12.6, 13.4 and 13.9 MV/m. The computed trajectories for electrons leaving a thermal emitter at $s = -7.2$ cm are drawn in Figure 5c. Contrary to field emission, all RF phases during the positive half wave are equally admissible for thermionic emission. The computed ΔT distribution from this thermal emitter for the four field levels is plotted in Figure 5d. It exhibits a peak in the hemisphere opposite to the emitter. This peak is observed in the measured temperature distribution but there is an additional peak near the emitting site. The most obvious explanation for this warmer region is direct heating of the cavity surface by the hot particle. This effect is not included in the simulation.

3.4 Distinction Between Field and Thermionic Emitters

A standard method for determining the unknown field enhancement factor β consists in measuring the electron current from a field emitter as a function of the local field E_0 and plotting the logarithm of $j_{FE}/E_0^{2.5}$ against $1/E_0$. This is called a 'Fowler-Nordheim plot'. In the present experiment we have determined the temperature rise of the thermometers which is proportional to the electron current density j_{FE}, multiplied with the kinetic energy gained by the electrons which grows linearly with E_0. For this reason we plot $\ln(\langle\Delta T\rangle/E_0^{3.5})$ versus $1/E_0$. For the data of Figure 4b the plot is shown in Figure 6a. An almost linear relationship is observed from which one derives a field enhancement factor $\beta \approx 190$.

For the thermionic emitter of Figure 5 one should, according to Equation (5), plot $\ln(\langle\Delta T\rangle/E_0^5)$ versus $1/E_0^2$ and use only the temperature data in the hemisphere opposite to the emitter since the energy deposited close to the emitting site is most likely due to direct heating. The resulting 'Richardson plot' is shown in Figure 6b. Also here the data are described quite well.

In practice it is difficult to decide from the Fowler-Nordheim or the Richardson plot whether a measured temperature increase is caused by field or thermionic emission. In Figures 6c, 6d we have purposely analyzed the previous data in the opposite way, the field emitter is treated as a thermionic emitter and vice versa. Apparently these fits are not bad either. If two peaks are observed along the meridian, thermionic emission is the preferred interpretation.

There may be cases where both effects are contributing. For instance it is conceivable that a sharp tip starts field emission; with increasing field strength it is heated up until the tip melts and field emission stops but the site has become so hot that it continues to release electrons via thermionic emission.

3.5 Cures Against Emission Sites

Absolute cleanliness during the various stages of cavity handling (heat treatment, chemical etching, water rinsing and assembly) is the prerequisite for achieving good performance. With these measures the field emission threshold is usually pushed beyond $E_{acc} \geq 10$ MV/m. High-pressure water rinsing reduces the emitter density. A technique for improving the performance of a cavity already installed in the cryostat is high peak power

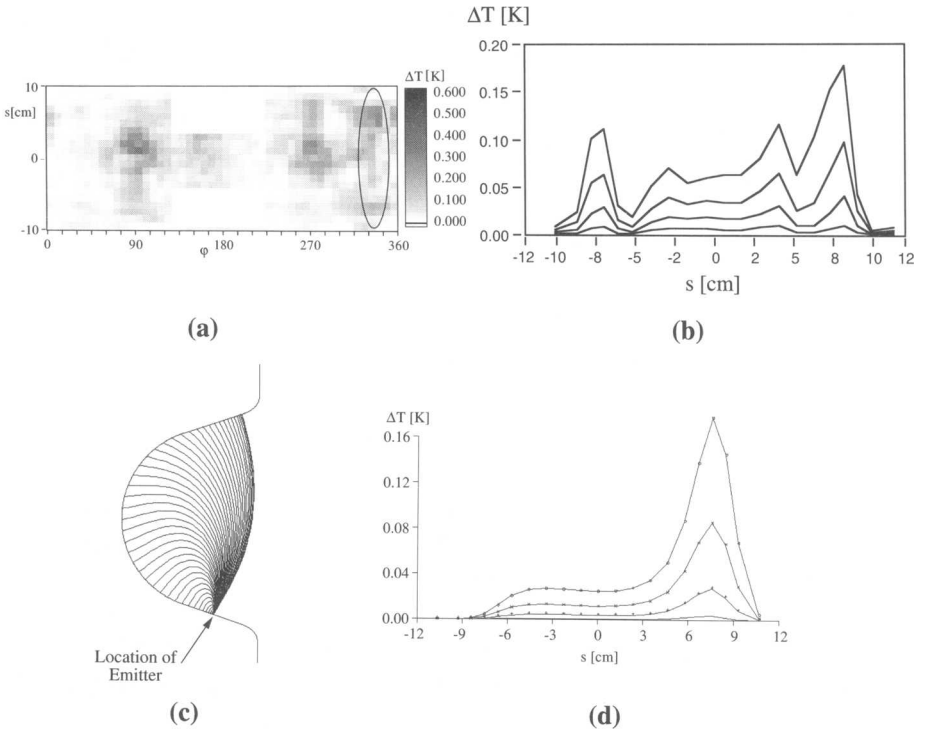

FIGURE 5 (a) Temperature map with a candidate for thermionic emission. (b) Heating along the 340° meridian for field levels of E_{acc} = 11.5, 12.6, 13.4 and 13.9 MV/m. (c) Trajectories for thermionic emission at $s = -7.2$ cm. All phases during the positive half wave of the RF are taken into account. The calculation was done for a field $E_{acc} = 13.9$ MV/m. (d) Calculated temperature distribution on the outer cavity surface for this thermionic emitter at the same field levels as in (b).

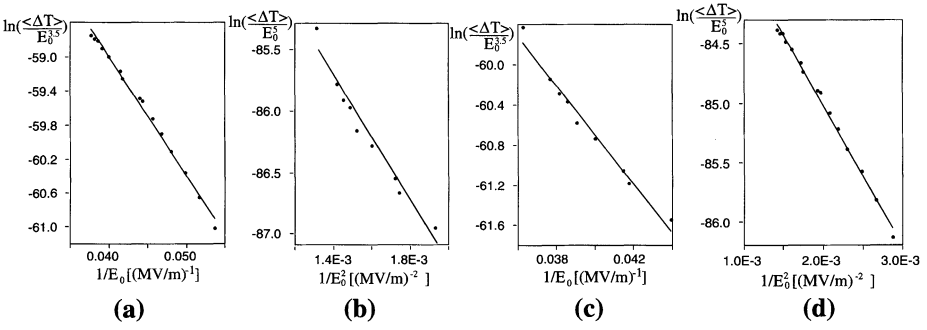

FIGURE 6 (a) Fowler-Nordheim plot for the field emitter of Figure 4. (b) Richardson plot for the thermionic emitter shown in Figure 5. (c) Fowler-Nordheim plot for the thermionic emitter. (d) Richardson plot for the field emitter.

processing (HPP).[3–5] The input coupler is moved further into the cavity beam pipe to get strong overcoupling and a fast rise of the cavity field. Then RF pulses of high instantaneous power (several hundred kW for a single-cell cavity) are applied whose duration is so short ($\leq$ 1 ms) that a general thermal breakdown is avoided. The rapidly rising field causes strong electron emission at field emitters and heats the sites so violently that they melt or evaporate. After high peak power processing an emitter has usually disappeared and the cavity can be excited to higher fields in normal cw operation.

4 EVOLUTION OF THE EMISSION CHARACTERISTIC DURING RF TESTS

4.1 First Test Sequence

The initial excitation curve $Q_0(E_{\mathrm{acc}})$ of the cavity in the first test sequence is presented in Figure 7. The temperature maps corresponding to the labeled points in Figure 7 are shown in Figure 8.

Starting from a quality factor $Q_0 = 1.8 \cdot 10^{10}$ the curve stays flat up to 8 MV/m (point 1). Map 1 reveals an area of about 15 cm^2 with an increased surface resistance which, from the measured dissipated energy, can be estimated to be in the order of 500 nΩ. The drop of Q_0 towards higher fields is associated with the appearance of a field emitter at the lower iris at $\varphi = 170°$ which is clearly visible in the second temperature map. Increasing the field to 14 MV/m opens another emitter at $\varphi = 75°$ (map 3). A small additional rise of the incident RF power leads to a discontinuous change in the excitation curve: in two steps point 4 is reached which has nearly the same Q_0 value as point 3 but at a higher field. The temperature map 4 reveals the origin of this improvement: the second emitter has disappeared. This is an example of 'low-power' processing (the cavity was powered with the 250 W amplifier in cw mode). Map 4 shows another remarkable feature: at the azimuthal position of the processed emitter an area of increased heat generation has been created near the equator. From the reduction in quality factor the surface resistance is estimated to be $\approx$ 600 nΩ. A possible explanation is that material evaporating from the emitter was deposited in this area and contaminated the surface. Returning to low field shows a clear Q_0 degradation to $7 \cdot 10^9$; basically the whole excitation curve $Q_0(E_{\mathrm{acc}})$ has been moved downwards but extends now to somewhat higher fields than before. The strong emitter was not affected by the available low-power RF field.

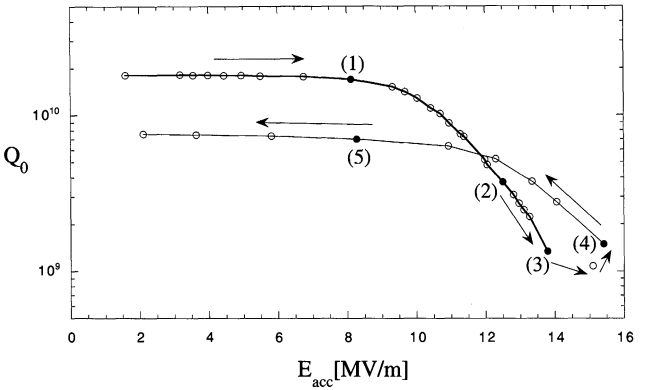

FIGURE 7 Excitation curve $Q_0(E_{acc})$ of the cavity during the first test directly after cooldown to 1.5 K.

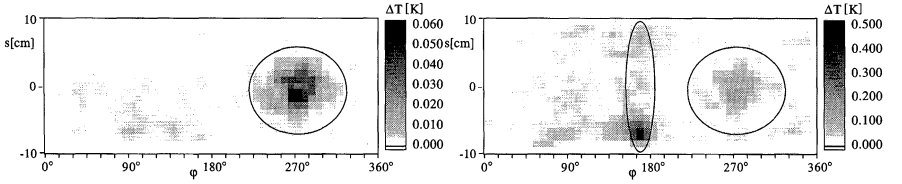

(1) E_{acc} =8.1 MV/m , Q_0=1.7·10^{10} (2) E_{acc} =12.5 MV/m , Q_0=3.7·10^{10}

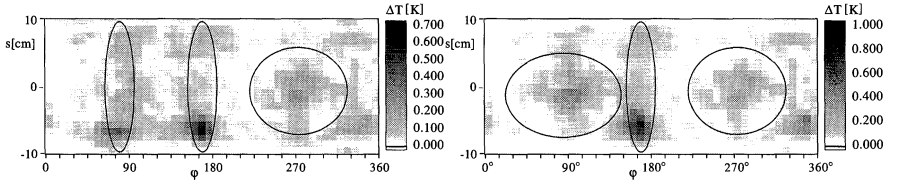

(3) E_{acc} =13.8 MV/m , Q_0=1.3·10^9 (4) E_{acc} =15.4 MV/m , Q_0=3.8·10^9

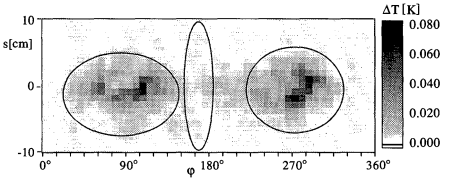

(5) E_{acc} =8.3 MV/m , Q_0=7.0·10^9

FIGURE 8 Temperature maps taken at the numbered points of the measurement in Figure 7.

This measurement series shows that processing of emitters may be accompanied with a Q_0 degradation due to surface contamination.

Since the strong emitter and some other emitting sites could not be removed with an RF power of 250 W it was decided to apply high peak power processing. Owing to a superfluid-helium leak in the waveguide HPP had to be performed at 4.2 K. The peak power was 250 kW at a pulse length of 2 ms.

In the subsequent low-power test in cw mode the top excitation curve in Figure 9 was obtained which has two remarkable features: the original Q_0 has been completely recovered and the excitation curve stays flat up to 14 MV/m. The temperature maps 1 and 2 (Figure 10) demonstrate that the strong emitter of the first test sequence has been eliminated by HPP. In addition the areas of increased surface resistance (map 5 in Figure 8) have disappeared. (The reason may be surface heating in the HPP procedure, accompanied with degassing).

With increasing field, $Q_0(E_{\text{acc}})$ follows a smooth excitation curve up to point 2 at 18.6 MV/m and $Q_0 = 4.4 \cdot 10^9$ where temperature map 2 reveals a hot spot near the equator at $\varphi = 300°$. Just above this point a jump is observed leading to point 3 on the second $Q_0(E_{\text{acc}})$ curve; the much reduced performance is caused by the emitter shown in map 3.

The second $Q_0(E_{\text{acc}})$ curve can be traced out reversibly but going beyond point 3 leads to a genuine low-power processing event: there is a discontinuous transition to point 4 at almost constant Q_0 but with a significant increase in field. Temperature map 4 shows that the emitter seen in map 3 has been removed. Instead a large region of increased surface resistance is observed. The third excitation curve can again be traced out reversibly. At low field the quality factor is appreciably lower than the initial value. A region of increased surface resistance is seen also here (map 5) and explains the Q_0 degradation (compare map 1). This is another example that processing of an emitter may be accompanied with a reduction of the low-field quality factor.

In addition to this test HPP was performed again at 4.2 K, this time with 500 kW pulses of 1 ms length. The quality factor at low field again recovered to $2.5 \cdot 10^{10}$, but after a processing event which took place at a field value of $E_{\text{acc}} = 21$ MV/m, the low field Q_0 reduced to $9 \cdot 10^9$ and a new region with high surface resistance was created. The cavity now showed thermal breakdown at 20 MV/m.

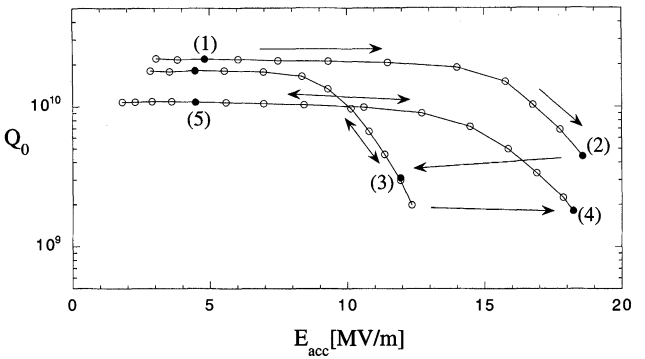

FIGURE 9 Q_0 versus E_{acc} behaviour at 1.5 K after applying high peak power processing at 4.2 K.

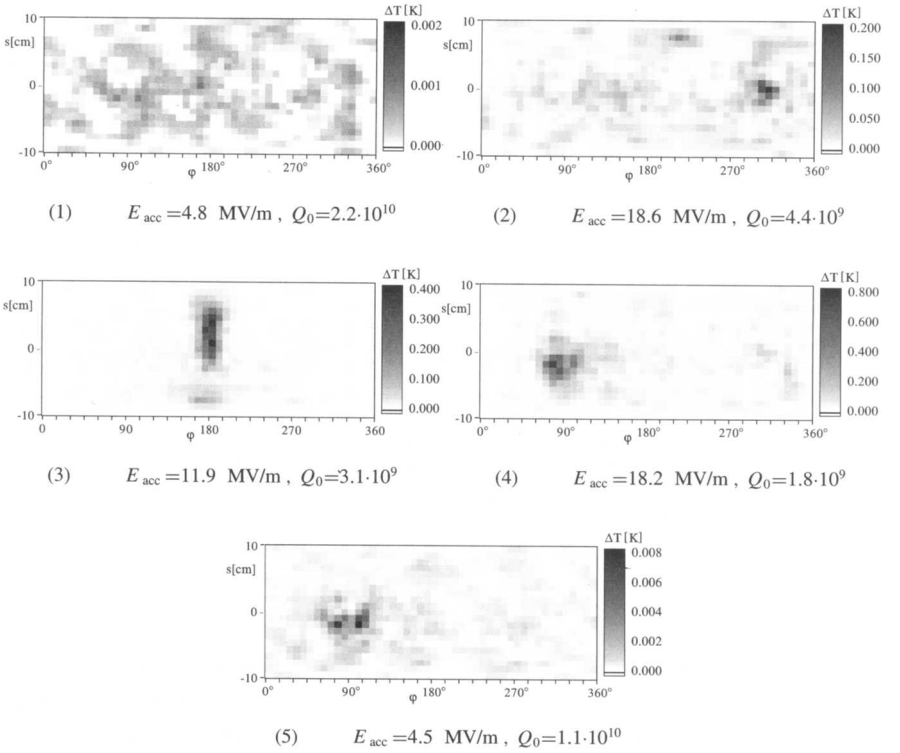

FIGURE 10 Temperature maps taken at the labeled points of Figure 9.

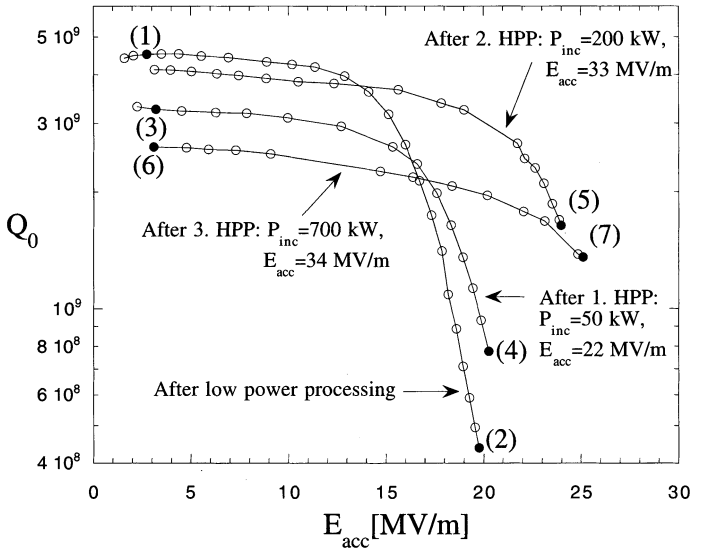

FIGURE 11 Q_0 versus E_{acc} measurements after various HPP sessions during the second test sequence.

4.2 Second Test Sequence

After a new chemical etching of the inner surface (15 μm removal) a second test sequence was performed. The cavity started with a low-field Q_0 of $2.5 \cdot 10^{10}$ and reached 19.5 MV/m with low-power conditioning. The processing generated again regions with higher surface resistance which degraded the quality factor to $4.5 \cdot 10^9$ at low field (Figure 11 and map 1, Figure 12). At the highest fields three emitters were present (map 2 of Figure 12).

Now HPP was carried out at 1.5 K. At an incident power of $P_{inc} = 50$ kW a processing event occurred, characterized by a decay of the transmitted-power signal in less than 1 μs. The excitation curve measured directly after this processing event in cw operation (Figure 11) showed a further reduction in the low-field quality to a value $Q_0 = 3.3 \cdot 10^9$. Temperature map 3 shows a new region with high surface resistance. Map 4, taken at high field, proves that two emitters were destroyed during the processing event but the emitter at $\varphi = 260°$ remained active.

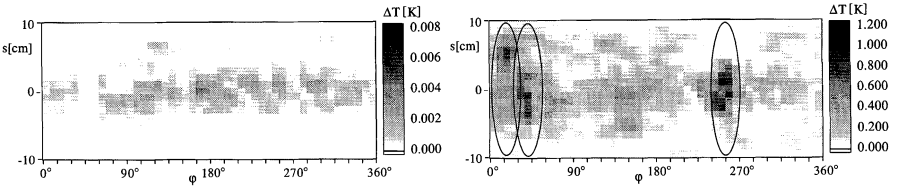

(1) E_{acc} =2.8 MV/m , Q_0=4.5·10^9

(2) E_{acc} =19.8 MV/m , Q_0=4.4·10^8

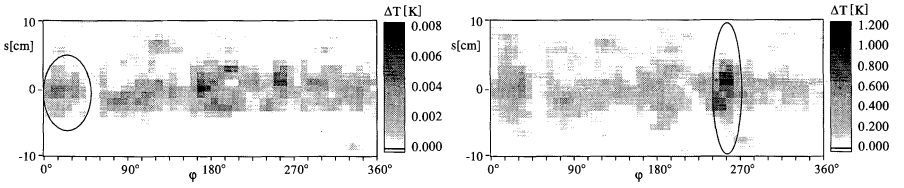

(3) E_{acc} =3.2 MV/m , Q_0=3.3·10^9

(4) E_{acc} =20.3 MV/m , Q_0=7.8·10^8

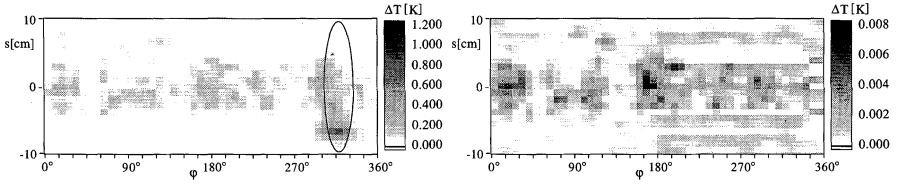

(5) E_{acc} =24.0 MV/m , Q_0=1.6·10^9

(6) E_{acc} =3.1 MV/m , Q_0=2.6·10^9

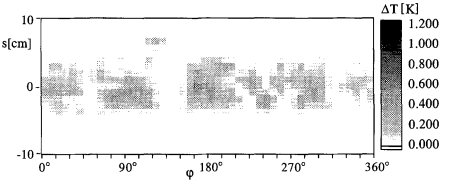

(7) E_{acc} =25.1 MV/m , Q_0=1.4·10^9

FIGURE 12 Temperature maps taken during the measurement of Figure 11.

Raising the klystron power to 200 kW in the next HPP step resulted in more than 20 processing events. A remarkable result of the following cw excitation curve was that in this case HPP increased the low-field quality factor from $3.3 \cdot 10^9$ to $4.0 \cdot 10^9$ at $E_{acc} = 3.1$ MV/m. Map 5 shows that the emitter at $\varphi = 260°$, visible in map 4, was destroyed by HPP but a new emitter opened at $\varphi = 330°$, limiting the field to $E_{acc} = 23$ MV/m.

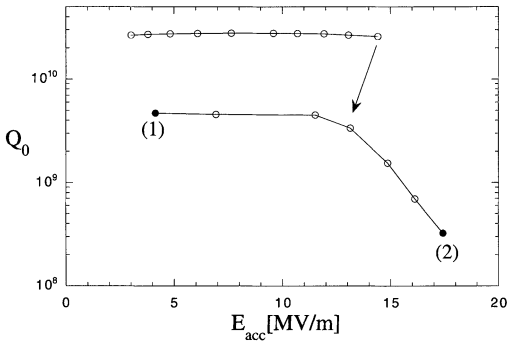

FIGURE 13 Q_0 versus E_{acc} measurement during the second test sequence after warming up the cavity to room temperature and cooling down again.

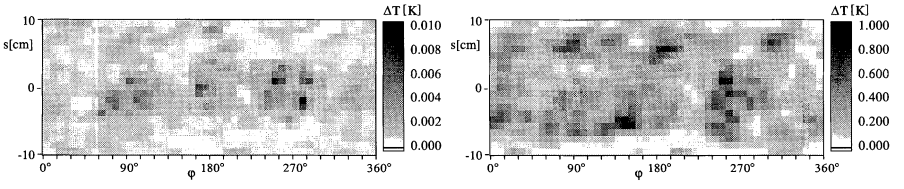

(1) E_{acc}=4.2 MV/m , Q_0=4.7·10^9 (2) E_{acc}=17.4 MV/m , Q_0=2.9·10^8

FIGURE 14 Temperature maps for the labeled points in Figure 13.

A last HPP session was carried out with a klystron power of up to 700 kW at 250 μs pulse length, during which the cavity reached 34 MV/m. This reduced the low-field Q_0 to 2.6 · 10^9 (map 6). The highest attainable field was 25.1 MV/m, limited by thermal breakdown. No more emitters were visible now, see map 7. The exitation curve $Q_0(E_{acc})$ could be traced out reversibly.

After this test sequence the whole system was warmed up to room temperature, pumped over the weekend and cooled back to 1.5 K. At the beginning the cavity had a quality factor of $Q_0 = 2.7 \cdot 10^{10}$ up to a field level of 14.4 MV/m (Figure 13) without indication of significant heating (less than 20 mK) in the temperature map. Trying to reach higher fields resulted in an erratic response of the cavity, not shown in Figure 13. Finally a stable excitation curve was reached with a low-field $Q_0 = 4.7 \cdot 10^9$ (map 1 in

Figure 14) and a highest accelerating gradient of 17.4 MV/m. At this field level, the corresponding temperature map 2 shows a strong heating of almost the entire cavity surface.

5 CONCLUSIONS

The tests described above were carried out on a single-cell cavity which contained a certain amount of contaminants due to vacuum leak problems. The results are not representative for the performance that can be achieved under best clean room conditions. Rather these investigations illustrate the capabilities of a temperature mapping system covering almost the entire cavity surface and its use in investigating low- and high-power processing of emitters. High peak power processing usually raised the attainable accelerating field but in most cases a reduction in quality factor was observed. Regions with increased surface resistance were found as a consequence of processing, indicating that material evaporated from the emission sites contaminated the surface. Warming up removed most of these lossy regions. Further studies are needed to determine the nature of the contaminants.

References

[1] W.-D. Möller, *Quest for High Gradients*, Proceedings of the 7th Workshop of RF Superconductivity, Saclay, France, 1995.

[2] J. Knobloch, *et al.*, *Design of a High Speed, High Resolution, Thermometry System for 1.5 GHz Superconducting Radio Frequency Cavities*, Review of Scientific Instruments, **65**(11), p. 3521 (1994).

[3] J. Graber, *et al.*, Proc. of the 1993 Particle Accelerator Conference, Washington, DC (IEEE Cat. No. 3279-7, p. 886, 1993).

[4] J. Graber, *High Power RF Processing Studies of 3 GHz Niobium Superconducting Accelerator Cavities*, Dissertation, Cornell University, Ithaca, NY, 1993.

[5] C. Crawford, *et al.*, *High Gradients in Linear Collider Superconducting Accelerator Cavities by High Pulsed Power to Surpress Field Emission*, Particle Accelerators, 1995, Vol. 49, pp. 1–13.